RSC Advances

PAPER

View Article Online
View Journal | View Issue

Cite this: *RSC Adv.*, 2021, **11**, 37276

Green construction of eco-friendly phosphotungstic acid Sr-MOF catalysts for crystal violet removal and synthesis of coumarin and xanthene compounds†

Amr A. Ibrahim, Shaimaa L. Ali, Mina Shawky Adly, S. A. El-Hakam, S. E. Samra and Awad I. Ahmed *

There is an urgent need to improve engineering and synthetic chemistry, either through the use of eco-friendly starting materials or the proper design of novel synthesis routes. This reduces the contamination of toxic chemicals and helps the disposal of organic dyes. In the current work, a metal–organic framework-based Sr(II) was fabricated to achieve the desired goal for dye removal and catalysis. Sr-MOF-based phosphotungstic acid (PWA/Sr-MOF) was hydrothermally synthesized to study its adsorption and catalytic activities. Remarkably, about 99.9% of crystal violet (CV) dye was removed using PWA/Sr-MOF within 90 min at room temperature. Various factors have been studied to investigate the optimum conditions such as pH of solution, initial dye concentration, contact time, and temperature. The maximum adsorption capacity of CV dye was reached after 90 min and well fitted the pseudo-second kinetic order and Langmuir adsorption isotherm. Coumarin and xanthene reactions were chosen to test the catalytic activity of the prepared PWA/Sr-MOF at 373 K. Furthermore, structural and chemical characterization of the fabricated samples was obtained using FT-IR, XRD, TGA, DTA, TEM, EDX, and XPS. PWA/Sr-MOF can be considered as a promising and green framework in the material design used to study catalytic and adsorption performances.

Received 24th September 2021
Accepted 11th November 2021

DOI: 10.1039/d1ra07160b

rsc.li/rsc-advances

1. Introduction

Over the past few decades, a new class of zeolite-like hybrid solids called metal–organic frameworks (MOFs) has attracted more attention in industrial and academic research.[1] These preeminent new spongy materials are designed and built from the linkage of metal ions or clusters and multi-dentate organic ligands *via* strong bonds. Much research work is concentrated on the investigation of MOFs due to their intrinsic structural properties.[2] Due to their unique features, MOFs show a highly considerable role in diverse fields like gas storage,[3,4] catalysis,[5] adsorption,[6] CO_2 capture,[7] sensors,[8] optical materials,[9] oxygen reduction,[10] ion exchange,[11] hydrogen energy conversion,[12,13] drug delivery,[14] *etc.* Because of the unique coordination requirements of the metal ion and the bulkiness of the interacting organic ligand, stereochemical issues might arise from the assembly of numerous compounds in a MOF structure.[15] Artlessly, MOFs recap the charm of spongy chemical structures. In the catalysis field, interesting possibilities may be opened by MOFs since they can cover the gap between crystalline heterogeneous and homogeneous catalysts through single active sites.[16]

Dyes attract more awareness as one of the most hazardous pollutants, which spoil the productivity of soil that cause various serious socioeconomic dilemmas and health hazards.[17] Throughout the years, several techniques, such as adsorption, chemical deposition, ionic exchange, solid–liquid phase extraction, photocatalytic degradation, coagulation, membrane, and electrochemical systems have been used.[18–28] Adsorption is vastly avowed as the most auspicious and efficient technique because of its low cost/capital invested, insensitivity to toxic substances, simplicity of design, and proficiency of the operation. In the latest years, nanotechnology has introduced a bountiful of novel nanomaterials that can exhibit promising

Chemistry Department, Faculty of Science, Mansoura University, Mansoura, Egypt. E-mail: awahmed@mans.edu.eg

† Electronic supplementary information (ESI) available: Thermal analysis of (a) pure Sr-MOF, (b) 5, (c) 25 and (d) 55 wt% PWA/Sr-MOF (Fig. S1), XRD of pure phosphotungstic acid (PWA) (Fig. S2), XPS survey spectrum of Sr-MOF and high resolution XPS of (b) C 1s, (c) N 1s, (d) O 1s, (e) P 2p and (f) Sr 3d (Fig. S3), energy-dispersive X-ray spectroscopy analysis data of Sr-MOF and 25 wt% PWA/Sr-MOF (Tables S1 and S2), respectively, energy-dispersive X-ray spectroscopy of (a) Sr-MOF and (b) 25 wt% PWA/Sr-MOF (Fig. S4), linear forms of (a) Langmuir, (b) Freundlich and (c) Temkin adsorption isotherms of CV dye using Sr-MOF and 25 wt% PWA/Sr-MOF adsorbents (Fig. S5), (a) pseudo-first order and (b) pseudo-second order kinetics isotherms for CV dye adsorption on various wt% of PWA/Sr-MOF (Fig. S6) and thermodynamic plots of (a) log k *versus* $1/T$ and (b) Gibbs free energy change (ΔG°) *versus* temperature (K) of CV dye adsorption onto 25 wt% PWA-Sr-MOF (Fig. S7). See DOI: 10.1039/d1ra07160b

effects on environmental treatment and clean-up.[29] Crystal violet dye is introduced into natural water by the sewage of the textile, medical and biotechnology industries, and paints.[30] The fabrication of bio-sorbent for CV removal was determined to be the most practical option among the numerous strategies used for dye removal.[31]

A coumarin derivative, 7-hydroxy-4-methylcoumarin, is frequently utilized used in fine chemical industries, such as the manufacture of insecticide hymecromone, which is employed as a starting material.[32] Currently, the Pechmann reaction is considered a suitable method for coumarin synthesis because of its mild reaction conditions, simple starting materials, and high product yields in short reaction time. Therefore, the focus of recent research has been on employing prepared heterogeneous catalysts for Pechmann condensation.[33] Additionally, xanthene compounds, exceptionally 14-phenyl-14*H*-dibenzo[*a*,*j*] xanthene, have acquired high solicitude from the biopharmaceutical production industries. They are distinguished by biological and pharmacological features, like antibacterial, anti-inflammatory,[34] antiviral,[35] and antifungal activities,[36] dyes,[37] photodynamic therapy.[38] Xanthene compounds have been produced using a variety of catalysts, including Fe_3O_4-HAD-SO_3H, sulfamic acid/CrMIL-101, sulfated starch, ZrO_2, and WO_x/ZrO_2.[39] Yet many preparation methods have drawbacks, such as restrictions on catalyst reusability, the use of hazardous solvents, the separation of pure products, long reaction time, and challenging workup.[40]

Herein, we report a novel material that has catalytic and adsorption activities. The green route followed in the synthesis of metal–organic frameworks-based Sr(II) using unhazardous organic linkers showed extensive properties. The catalytic activity of Sr-MOF-supported PWA was examined on the synthesis of xanthene and coumarin derivatives besides the adsorption of CV dye. The prepared substances were investigated by various techniques for characterization like FT-IR, XRD, XPS, DTA, TEM, TGA, and EDX analysis. The effects of pH, concentration, contact time and reusability on CV dye adsorption have all been investigated.

2. Experimental

2.1. Materials

All chemicals utilized in the elaboration of substances such as strontium nitrate ($Sr(NO_3)_2$), oxalic acid ($C_2H_2O_4$), orthophosphoric acid (H_3PO_4), urea ($CO(NH_2)_2$), crystal violet ($C_{25}N_3H_{30}Cl$) dye, and phosphotungstic acid ($H_3PW_{12}O_{40}\cdot 12H_2O$) have been typically purchased from Alfa Aesar without any further purification.

2.2. Synthesis of Sr-MOF

Sr-MOF was synthesized by hydrothermal method from a mixture of strontium nitrate, orthophosphoric acid, oxalic acid, and urea with a molar ratio of 0.94 : 5.6 : 1 : 3, respectively, dissolved in DI water. The solution was stirred for 1 h then transferred into a stainless-steel Teflon tube and heated at 373 K for 72 h. Subsequently, the Teflon tube was allowed to cool at room temperature and the product was collected by centrifuge and washed repeatedly with DI water. Finally, the resulted powder was dried overnight in a conventional oven at 353 K.

2.3. Synthesis of PWA/Sr-MOF

Different weight percentages of PWA (5, 10, 15, 25, 35, 45, 55, and 65 wt%) were loaded on Sr-MOF by the impregnation method. Typically, 1.0 g of Sr-MOF was dispersed well with the calculated masses of PWA in 20 mL DI water. The suspension was stirred for 24 h then impregnated for 48 h at 298 K. Several washes were performed on the powder using DI water then dried in a conventional oven at 353 K.

2.4. Acidity measurements

The total acidities of the resulted catalysts were known and established by a simple titration approach using potentiometric titration. Typically, after activating the catalysts at 373 K for 2 h, 50 mg of each catalyst was homogeneously dispersed in acetonitrile and stirred for 3 h. The titration procedure was performed at a rate of 0.05 mL min^{-1} against 0.01 N *n*-butylamine.[41] The acidic sites of the synthesized catalysts were determined from the ratio between Brønsted and Lewis acid sites that were given from the FT-IR spectra of the adsorbed pyridine. The catalysts were kept in touch with the vapor of pyridine, for 30 days.

2.5. Characterization

The samples were thermally investigated using a Shimadzu thermal analyzer under N_2 atmosphere at a flow rate of 20 mL min^{-1} and a heating rate of 10 °C min^{-1}. FT-IR spectra were performed by utilizing Nicolet Magna IR 550 at the resolution of 4 cm^{-1}. XRD spectra were obtained with a Cu target on a PW 150 Philips Materials Research diffractometer at angle range from 10 to 50°. XPS data were collected by utilizing K-ALPHA with monochromatic X-ray Al K-alpha radiation (Thermo Fisher Scientific, USA) at a pressure of 10^{-9} mbar. TEM images were obtained using JEOL-JEM-2100 at a power of 120 kV and EDS data were collected by using an X-ray analyzer of JEOL-JSM-6510lv scanning electron microscope with a resolution of 1 pÅ to 1 μÅ. Surface zero net charges (pH_{PZC}) were studied using a series of solutions. Generally, 0.15 g of each catalyst was suspended in six bottles containing 50 mL KCl (0.1 N). Each solution's pH was adjusted with dilute solutions of HNO_3 and NaOH at values of 2, 4, 6, 8, 10, and 12 (pH_i). Then, for 24 h at room temperature, the bottles were then shaken to achieve equilibrium. Consequently, the pH within each solution was determined again and a relation was plotted between the initial pH (pH_i) against ΔpH.[42]

2.6. Batch equilibrium studies

Batch adsorption experiments were carried out using 50 mg of adsorbent in 50 mL of CV dye. The mixtures were suspended using ultrasonic for few minutes then shacked for 90 min. The desired pH of solutions was adjusted by using diluted NaOH

and HCl solutions. The adsorption capacities and removal percentage were evaluated by applying the following eqn (1) and (2).

$$q_e = \frac{(C_o - C_e)V_{(L)}}{m_{(g)}} \quad (1)$$

$$\%\text{Removal} = \frac{C_o - C_e}{C_o} \times 100 \quad (2)$$

where; $V_{(L)}$ is the solution volume, C_o is the initial dye concentration (mg L^{-1}), C_e is the dye concentration at equilibrium (mg L^{-1}), and $m_{(g)}$ is the adsorbent mass.

2.7. Catalysis studies

2.7.1. Synthesis of 7-hydroxy-4-methylcoumarin. In the presence of a 50 mg active catalyst, ethyl acetoacetate (20 mmol) reacts with resorcinol (10 mmol). The reaction was conducted at 373 K for 2 h in an oil bath with constant stirring yielded 7-hydroxy-4-methylcoumarin. The catalyst was separated from the hot mixture in presence of ice cubes then stirred for 15 min before refiltration. Melting point and FT-IR were used to validate the product's existence.[43]

2.7.2. Synthesis of 14-phenyl-14*H*-dibenzo[*a*,*j*]xanthene. The reaction between β-naphthol (2 mmol) and benzaldehyde (1 mmol) with 50 mg of active catalyst was used to synthesize xanthene. The mixture was agitated for 2 h at 373 K and the reaction's progress was evaluated using thin-layer chromatography (TLC). Furthermore, the product was dissolved in ethanol and the reaction mixture was separated from the solid catalyst by filtration followed by washing with ethanol 3–4 times. Eqn (3) was used to estimate the target product's yield.

$$\text{Yield} = \frac{\text{Mass of obtained product}}{\text{Mass of theoretical product}} \times 100 \quad (3)$$

3. Results and discussion

3.1. Design and characterization

Thermogravimetric (TGA) analysis under N_2 atmosphere of the three samples 5, 25, and 55 wt% PWA/Sr-MOF was illustrated in Fig. S1 (ESI).† All samples showed high thermal stability till 500 °C and there was a sharp decrease in mass, which may be attributed to the destruction of MOF structure and loss of frame water trapped in PWA molecules.[44] DTA technique is traditionally used to determine the thermal processing of the samples. DTA curves confirm that the prepared materials have high thermal stability till 500 °C. Additionally, all curves illustrated endothermic peak at ~180 °C and exothermic peak at ~535 °C ascribed to the weight loss of water molecules and decomposition of MOF structure, respectively.

The FT-IR spectra for pure Sr-MOF and other catalysts are depicted in Fig. 1. Bands at 3360 and 3510 cm^{-1} are usually attributed to N–H and O–H stretching vibrations, respectively, implying that adsorbed water and urea groups have been a key component of the formation of OPA-MOF. The peaks at 2930 and 1630 cm^{-1} are ascribed to stretching vibrations of C–H and C=O, respectively, which confirm that oxalic acid was successfully introduced on the structure of frameworks. Because of the use of phosphoric acid in hydrothermal preparation, the stretching vibration of P–O was responsible for the peak at 915 cm^{-1}.[45] Four W_3O_9 groups formed by edge-sharing octahedra surround a PO_4 tetrahedron in the $PW_{12}O_{40}^{3-}$ Keggin anion configuration. Various bands attributable to different kinds of oxygen atoms may be seen in the fingerprint area between 1100 and 500 cm^{-1}. Five bands are observed at 1080, 984, 893, 781, and 597 cm^{-1} ascribed to stretching vibrations of P–O, W=O_t, W–O_c–W, W–O_e–W and the vibrational bending of P–O, respectively.[46]

XRD patterns were used to analyze the crystal structure of the prepared samples, as observed in Fig. 2. The main characteristic peak of Sr-MOF crystal was observed at an angle of 14.5°, endorsing the crystalline structure of the prepared frameworks. All the diffraction peaks of pure Sr-MOF have well corresponded to those in the 5 wt% PWA/Sr-MOF. The incorporation of PWA with high content slightly influenced the crystal structure of Sr-MOF. Additionally, the PWA clusters are dispersed homogeneously in the framework as their patterns were absent in these samples and the increase of PWA content did not impact the dispersion.[47] The XRD of pure phosphotungstic acid as illustrated in Fig. S3 (ESI).†

The elemental composition and bonding configuration of the catalysts were investigated using XPS, as illustrated in Fig. 3 and S3 (ESI).† Sr-MOF illustrated different five peaks attributed to C 1s, N 1s, O 1s, P 2p, and Sr 3d. This indicates that the reagents like oxalic acid, urea, phosphoric acid, and strontium chloride were involved in the formation of the frameworks and became part of their skeleton. High-resolution XPS of C 1s showed four peaks allocated at 284.5, 286.0, 288.5, and 290.9 eV ascribed to C–C, C–O, C=O, and O–C=O, respectively. Additionally, O 1s split into three peaks of O=C (531.4 eV), O–C (532.8 eV) as well as C–O–Sr (534.3 eV).[45] N 1s deconvoluted into

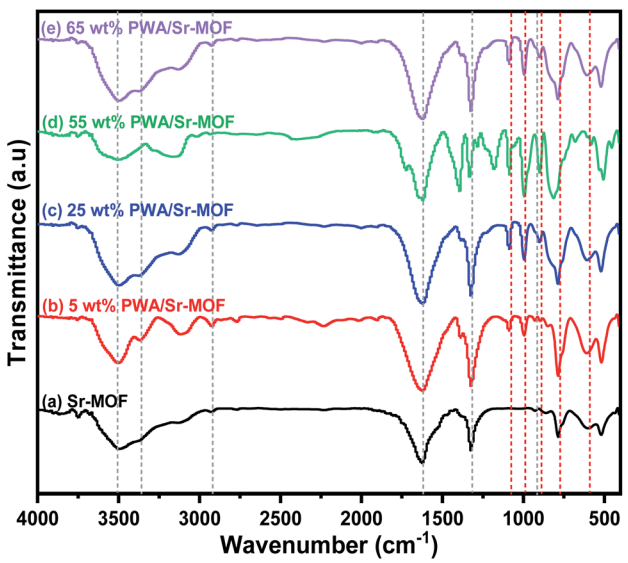

Fig. 1 FT-IR spectra of (a) Sr-MOF, (b) 5, (c) 25, (d) 55, (e) 65 wt% PWA/Sr-MOF.

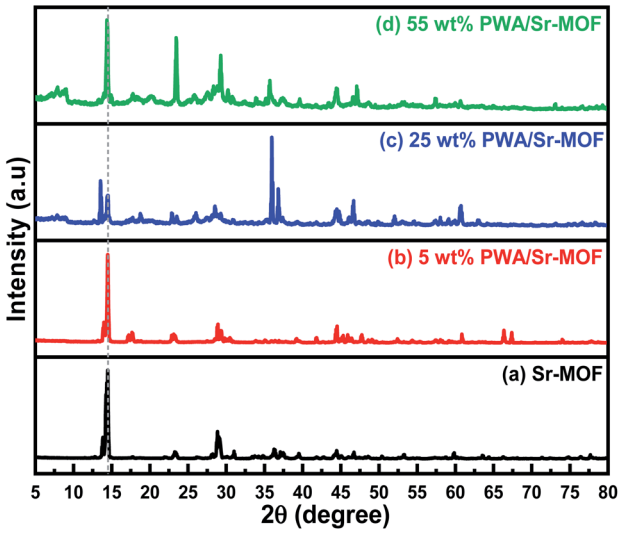

Fig. 2 XRD patterns of (a) pure Sr-MOF, (b) 5, (c) 25, (d) 55 wt% PWA/Sr-MOF.

two peaks placed at 401.4 and 407.0 eV corresponding to NH_2 and C–N, respectively.[48,49] High-resolution XPS of P 2p observed two peaks at 133.4 and 135.1 eV attributed to P $2p_{3/2}$ and P $2p_{1/2}$, respectively.[50] The deconvolution of Sr 3d showed two peaks at 135.2 and 133.5 eV assigned to Sr $3d_{3/2}$ and Sr $3d_{5/2}$, respectively.[51] The XPS spectrum of 25 wt% PWA/Sr-MOF showed essentially the same features except a new peak associated with W 4f. The high-resolution XPS of W 4f deconvoluted into four peaks at 36.1, 38.1, 38.7, and 42.0 eV associated with W $4F_{7/2}$, W $4F_{5/2}$, WO_3 and W 4P, respectively.

Transmission electron microscopy (TEM) images were captured for pure Sr-MOF, 5 and 25 wt% PWA/support. Fig. 4(a) shows TEM image of Sr-MOF that appeared as globular with a somewhat sponge structure. As illustrated in Fig. 4(b) and (c), the original bright image of the nanosheet pores darkened with increasing content of PWA, indicative of the increase in PWA-containing MOF coverage correctively. Furthermore, the distribution of PWA species within the MOF and the viability of the process were by the evident adhesion of the PWA with the interior/exterior of the MOF.

The energy-dispersive X-ray spectroscopy (EDS) of PWA/Sr-MOF indicates the presence of the five elements Sr, O, P, C, N, and W in a high peak shape. Fig. S4 (ESI†) illustrates the samples are not in a physical mixture but are in chemical interaction, which confirms the successful synthesis of the materials.[52] Tables S1 and S2 (ESI†) indicate the elemental analysis of Sr-MOF and 25 wt% PWA/Sr-MOF.

3.2. Surface acidity measurements

3.2.1. Potentiometric titration. Table 1 displays non-aqueous titration surface acidity readings for all prepared samples. The acid strength may be characterized using the following scale based on the initial potential of the non-aqueous suspensions: $E_i > 100$ mV (extremely strong sites), $100 > E_i > 0$ mV (strong sites), $0 > E_i > -100$ mV (weak sites) as well as -100 mV $> E_i$ (extremely weak sites).[41,53] Furthermore, the inflection point of the curve, which represents the titration's endpoint, is a reasonable metric for comparing the acidity of various samples. The initial electrode potential (E_i) was given as a gauge for interpreting the data. As a criterion for calculating the overall number of acidic sites, the value of $m_{equivalent}$ g^{-1} solid where the plateau has been attained was recommended, which is illustrated in eqn (4).

$$\text{Total number of acid sites per g} = \frac{m_{\text{equivalent}}\ g^{-1} \times N_A}{1000} \quad (4)$$

The potentiometric titration curves for the samples were shown in Fig. 5. With E_i value of 140 mV, the Sr-MOF support

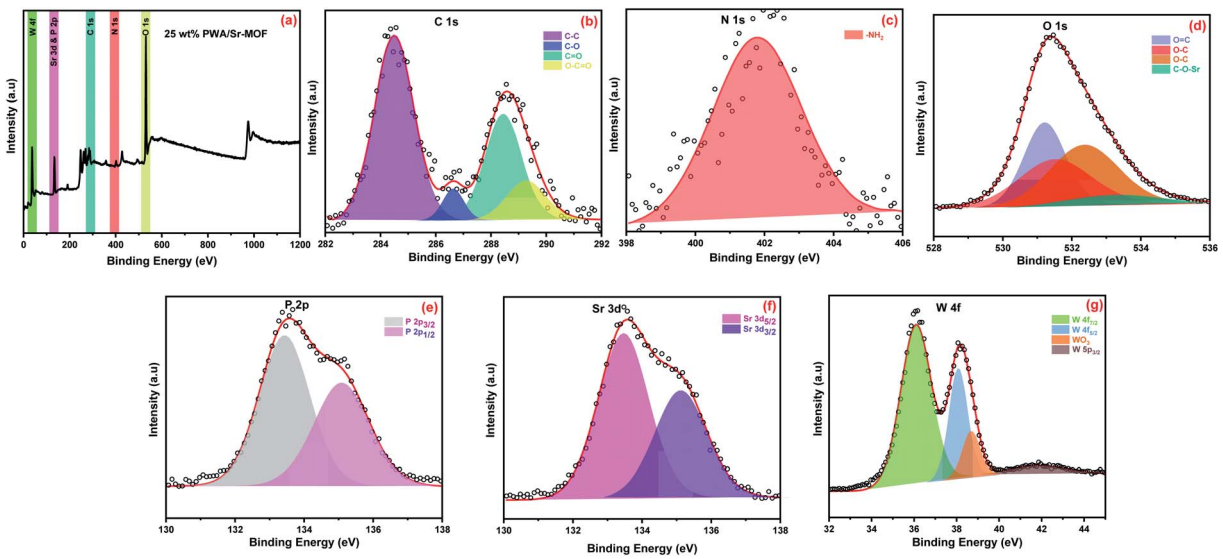

Fig. 3 (a) XPS survey spectrum of 55 wt% PWA/Sr-MOF and high resolution XPS of (b) C 1s, (c) N 1s, (d) O 1s, (e) P 2p, (f) Sr 3d and (g) W 4f.

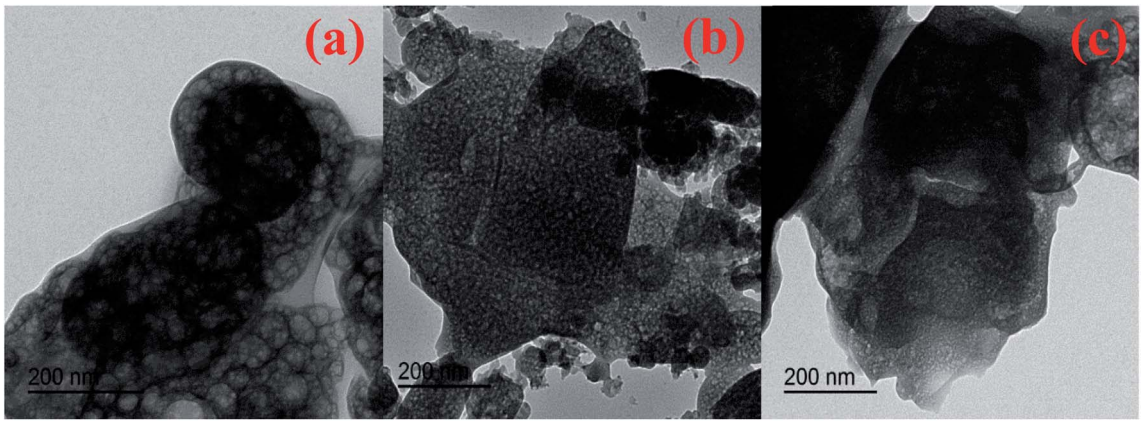

Fig. 4 Transmission electron microscopy images of (a) Sr-MOF, (b) 5 wt% PWA-Sr-MOF and (c) 25 wt% PWA-Sr-MOF.

Table 1 Acidic properties of Sr-MOF and PWA/Sr-MOF

Catalyst	E_i (mV)	No. of acid sites	$I_{B(1540)}$	$I_{L(1450)}$	I_B/I_L
Sr-MOF	140	0.028	3.23	3.29	0.98
5 wt% PWA/Sr-MOF	265.8	0.066	6.25	4.81	1.30
25 wt% PWA/Sr-MOF	426.7	1.49	8.76	5.69	1.54
55 wt% PWA/Sr-MOF	446.4	1.84	27.09	6.86	3.95
65 wt% PWA/Sr-MOF	434.9	0.976	13.24	5.95	2.73

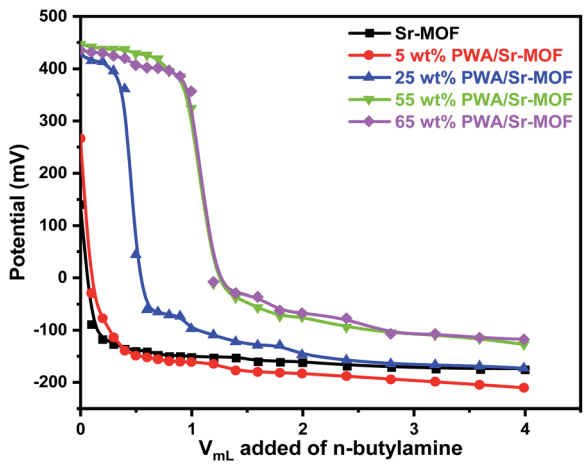

Fig. 5 Potentiometric titration curves of *n*-butylamine in acetonitrile for the different synthesized samples.

has a modest number of acid sites. As predicted, the addition of PWA resulted in a simultaneous rise in acid strength as well as the overall number of acid sites. The acidity reached the highest value at 55 wt% PWA with further increase of PWA content then decreased with 65 wt% PWA. The acidic property of pure Sr-MOF is attributed to the presence of phosphoric and oxalic acid in its structure, which is moderately acidic. Above the surface saturation coverage (65 wt%), the sample lost its acidity that could be directly linked to aggregation (Keggin–Keggin interactions) of the PWA species.[46]

3.2.2. Pyridine adsorption. Pyridine adsorption is a technique used to characterize both Brønsted (B) as well as Lewis acidic (L) sites in the supported PWA samples. The following sets of bands exhibit chemisorbed pyridine perhaps in the range of 1400–1700 cm^{-1}. Pyridium ion (PyH^+) and pyridine by Lewis acid sites (PyL) were placed at 1637 and 1622 cm^{-1}, respectively.[54] As noticed in Fig. 6, over both Brønsted and Lewis acid sites, the detected band at 1490 cm^{-1} is characteristic of the ν_{19a} mode.[55] The acidity of the prepared samples was affected by the amount of PWA loaded on the support surface. The B/L ratios were determined from the intensities between B and L acid sites positioned at 1622 and 1400 cm^{-1}, respectively. Both B and L acidities appeared at a low loading of PWA, which increased by increasing the loading content. The acid strength and surface acidity enhanced in case of incorporation of PWA till reached the maximum at 55 wt% PWA then decreased above this percent due to agglomeration that prevents pyridine molecules to access the active sites.

3.3. Adsorption studies

3.3.1. pH zero-point charge (pH_{ZPC}) measurements. pH_{zpc} of the prepared materials was investigated as reported by A. A. Ibrahim *via* electrochemical technique.[56] Series of KCl solutions (50 mL, 0.1 N) have been prepared and the initial pH of solutions was calibrated to various values ranging from 2 to 12. Afterward, 50 mg of each sample was added to the previous solutions and shaken for a couple of days. Relation between ΔpH ($pH_f - pH_i$) *versus* initial pH (pH_i) was plotted and the pH value passes through the initial pH line and is defined as pH_{zpc}. Fig. 7, observed the pH_{pzc} values of 6, 3.9, 3.15, and 3 for Sr-MOF, 5, 25, and 55 wt% PWA/Sr-MOF, respectively. The surface was positively charged (attracting anions) at $pH_i < pH_{pzc}$ and the positive surface charge of catalysts was decreased with increasing pH values. In contrast, PWA/Sr-MOF presented negative charges (attracting cations/repelling anions) at $pH_i > pH_{pzc}$ and the negative surface charges were increased with pH increase.

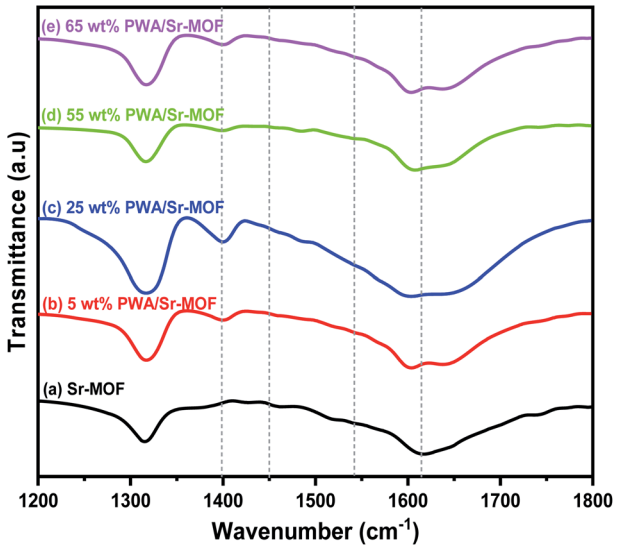

Fig. 6 FTIR spectra of pyridine adsorbed on the prepared samples.

3.3.2. Adsorption of crystal violet (CV) dye. The adsorption capacity has been swayed by the solution's pH, which is a key test and one of the most significant factors. The removal performance of CV dye was enhanced by increasing pH to a maximum at 7 as witnessed in Fig. 8(a). The adsorption capacity was enhanced by 14% from pH 3 to pH 7 using 25 wt% PWA/Sr-MOF. The pH_{zpc} value of the adsorbent was 3.15, which explains the low adsorption rate of cationic dyes as a result of competition between dye molecules and protons in the solution, especially at high concentrations.[57] Additionally, in an acidic medium, the hydronium ions have much mobility higher than dye molecules. On the other hand, the removal efficiency dimensioned at a high pH value due to the dye molecules are competed with HO^- ions.[58] Furthermore, a neutral solution (pH 7) was more favorable for CV dye adsorption at room temperature. Fig. 8(b) explains the impact of PWA loaded on the surface of Sr-MOF for the removal of CV dye. Sr-MOF-supported PWA

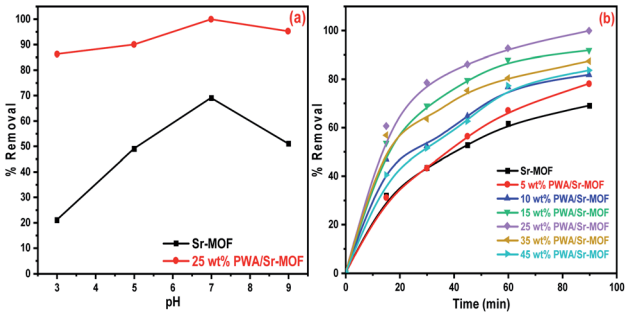

Fig. 8 (a) Effect of initial pH on adsorption capacities of CV dye from aqueous solution using Sr-MOF and 25 wt% PWA/Sr-MOF and (b) effect of PWA content loaded on Sr-MOF on adsorption of CV dye from aqueous solution. [Conditions: C_o = 100 mg L^{-1}, volume = 50 mL, adsorbent dose = 50 mg, contact time = 90 min, and T = 298 K].

samples exhibited higher adsorption capacities compared to pure MOF. The adsorption efficiency was increased by increasing the PWA content till achieved an upper limit at 25 wt% PWA. The adsorption capacity decreased above this content, which could be ascribed to the high PWA content distributed on the surface of frameworks may reduce the accessibility to the active sites.

The initial concentration influence was investigated using a series of CV solutions within the concentration range from 50 to 400 mg L^{-1}. As observed in Fig. 9(a), the removal efficiency enhanced as concentration increased till reaching the state of equilibrium saturation of 237 mg g^{-1}. At high concentrations, the adsorption capacity may be decreased due to the surface-active site saturation and interactions between dye molecules on the bulk and solid phases that could be repulsive.[59] In Fig. 9(b), the adsorption capacities were enhanced by raising the adsorbent dose from 0.6 to 1.8 mg L^{-1}. The considerable increase of dye removal was attributable to the great availability of active sites scattered across the surface of the adsorbent at a higher dosage.[60] Fig. 10 shows the influence of contact time on the removal of CV from an aqueous solution. It was clear that

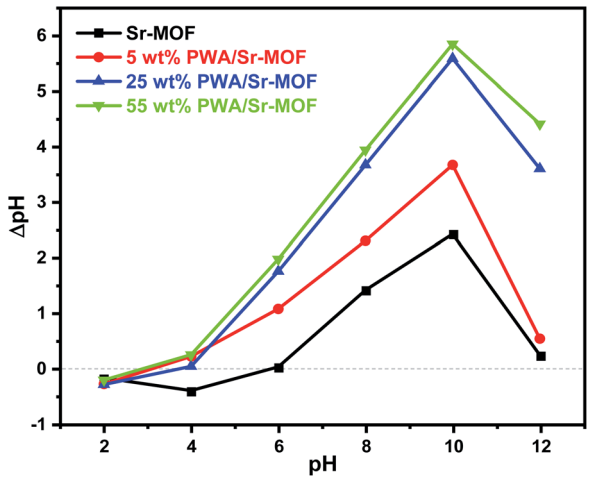

Fig. 7 Zero-point charge of pure Sr-MOF and the prepared catalysts.

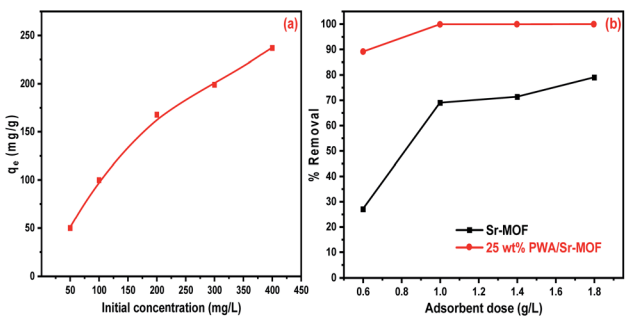

Fig. 9 (a) Effect of initial concentration on adsorption capacities of CV dye from aqueous solution using 25 wt% PWA/Sr-MOF, [conditions: C_o = 50–400 mg L^{-1}, volume = 50 mL, adsorbent dose = 50 mg, contact time = 90 min, pH 7 and T = 298 K] and (b) effect of adsorbent dose on adsorption capacities of CV dye from aqueous solution using Sr-MOF and 25 wt% PWA/Sr-MOF, [conditions: C_o = 100 mg L^{-1}, contact time = 90 min, volume = 50 mL, pH 7 and T = 298 K].

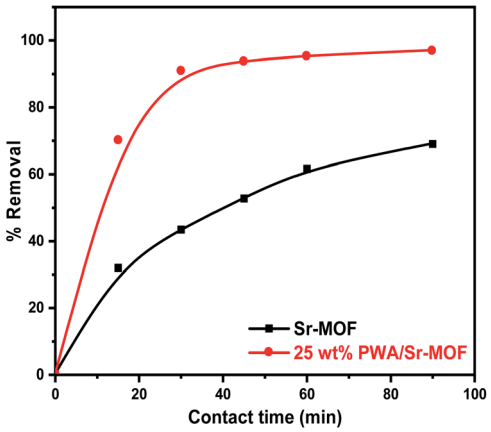

Fig. 10 Effect of contact time on adsorption of CV dye from aqueous solution by using Sr-MOF and 25 wt% PWA/Sr-MOF, [conditions: C_o = 100 mg L^{-1}, volume = 50 mL, adsorbent dose = 50 mg, T = 298 K and pH 7].

the removal percentage reached more than 91% after 30 min using 25 wt% PWA/Sr-MOF. In the case of Sr-MOF, about 32% of CV dye was adsorbed after the same contact time. The optimum temperature was applied to all adsorption experiments conducted at room temperature.

The recyclability experiments of pure Sr-MOF and 25 wt% PWA/Sr-MOF were conducted under the same conditions. The regeneration of the adsorbent was performed by separating the solids using a centrifuge followed by chemical treatment with HNO_3 (0.1 N) and allowed to dry in a conventional oven at 343 K. After the fourth cycle, the adsorption efficiency of CV dye using 25 wt% PWA/Sr-MOF dropped by 24% compared to 50% using pure Sr-MOF, as shown in Fig. 11. It is plausible to assume that the 25 wt% PWA/Sr-MOF produced is a potential adsorbent for dye adsorption.

3.3.3. Equilibrium adsorption isotherms. The experimental findings were analyzed using three distinct adsorption isotherms including Freundlich, Langmuir, and Temkin isotherms. The liner forms of these isotherms are given as follow:

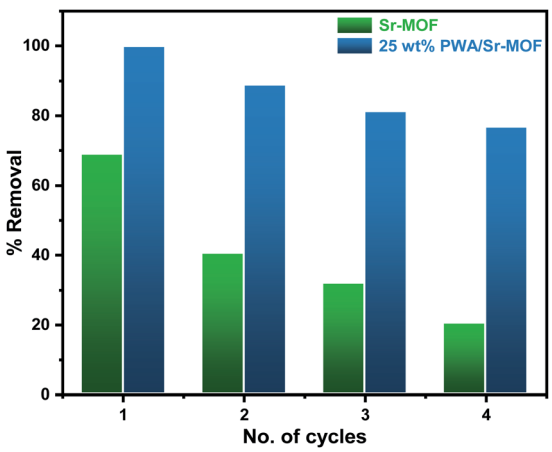

Fig. 11 Recyclability of Sr-MOF and 25 wt% PWA/Sr-MOF on CV dye adsorption from aqueous solution, [conditions: C_o = 100 mg L^{-1}, volume = 50 mL, adsorbent dose = 50 mg, contact time = 90 min, pH 7 and T = 298 K].

Langmuir adsorption isotherm:

$$\frac{C_e}{q_e} = \frac{1}{K_L q_m} + \frac{C_e}{q_m} \quad (5)$$

Freundlich adsorption isotherm:

$$\log q_e = \frac{1}{n}\log C_e + \log K_F \quad (6)$$

Temkin adsorption isotherm: where

$$q_e = \frac{RT}{b_T}\ln A_T + \frac{RT}{b_T}\ln C_e \quad (7)$$

as, q_m (mg g^{-1}) is for the highest possible amount of the dye adsorbed, K_L (L mg^{-1}) and K_F ((mg g^{-1})/(mg $mL^{-1})^{1/n}$) are the Langmuir and Freundlich constants, respectively, R is the universal gas constant (8.314 J mol^{-1} K^{-1}), n is a representation of the adsorption mechanism, A_T is the binding constant equilibrium of Temkin isotherm (L mol^{-1}), T is the temperature (K), and b_T is Temkin isotherm constant (J mol^{-1}).[61] The adsorption isotherm explains the behavior of any interaction between adsorbent and adsorbate molecules. The variables derived from the various models are used to identify surface properties and adsorbent affinity and propose a mechanism for the adsorption process. The Langmuir, Freundlich, and Temkin adsorption isotherms are all compared as demonstrated in Fig. S5 (ESI).† According to the data, the adsorption of CV dye on 25 wt% PWA/Sr-MOF was more fitted with the Langmuir than the Freundlich adsorption isotherm (Table 2). The Temkin isotherm indicates the heat of adsorption (whether it's endothermic or exothermic) and the adsorbate–adsorbent interaction.[62] The energy of adsrobed molecule is supposed to decrease linearly as the coverage increases. The heat of CV adsorption (b_T) is concerning the coverage of dye molecules on the PWA/Sr-MOF surface due to adsorbent–adsorbate interaction. The Temkin isotherm clearly shows that as the temperature raised from 298 to 338 K, the value of b_T increased that indicating the sorption was endothermic. The value of b_T was higher than 80 kJ mol^{-1}, which assumed the removal process was chemical and revealed strong ionic interaction between dye molecules and PWA/Sr-MOF surface.

3.3.4. Kinetic study of CV dye adsorption. Two kinetic models were previously used to evaluate the rate data to fully know adsorption mechanisms such as mass transfer and chemical reaction. The batch adsorption method is being studied to see if it can be used for wastewater treatment. To assess the possible mechanism implicated in the adsorption process, pseudo-second and pseudo-first kinetic models were applied to study the adsorption rate.[63,64]

Pseudo-first order

$$\ln(q_e - q_t) = \ln q_e - k_1 t \quad (8)$$

Pseudo-second order

Table 2 Langmuir, Temkin and Freundlich adsorption isotherms constants for the adsorption of CV dye

		Langmuir isotherm				Freundlich isotherm			Temkin isotherm			
Adsorbent	q_m, exp (mg g^{-1})	K_L (L mg^{-1})	b (L mg^{-1})	q_m, calcd (mg g^{-1})	R^2	K_f ((mg g^{-1})/(mg $mL^{-1})^{1/n}$)	n	R^2	b_T (J mol^{-1})	A_T (L mol^{-1})	R^2	B
Sr-MOF	69.0	0.193	16.5	71.11	0.98	3.2	2.21	0.97	164.1	12.1	0.92	15.1
25 wt% PWA/Sr-MOF	237.0	1.07	50.4	244.29	0.99	120.47	9.09	0.96	183.7	140.4	0.93	13.5

Table 3 Kinetic parameters of the pseudo-second and pseudo-first orders for adsorption of CV dye

			Pseudo-first order		Pseudo-second order	
Adsorbent	C_o (mg L^{-1})	q_e, exp (mg g^{-1})	k_1 (min^{-1})	R^2	$k_2 \times 10^{-3}$ (g mol^{-1} min^{-1})	R^2
Sr-MOF	100	69.00	0.001	0.888	0.05	0.989
5 wt% PWA/Sr-MOF	100	78.11	0.149	0.956	6.29	0.996
10 wt% PWA/Sr-MOF	100	81.80	0.165	0.985	6.67	0.995
15 wt% PWA/Sr-MOF	100	91.84	0.174	0.965	7.30	0.993
25 wt% PWA/Sr-MOF	100	99.95	0.313	0.995	7.47	0.999
35 wt% PWA/Sr-MOF	100	87.42	0.196	0.921	7.11	0.998
45 wt% PWA/Sr-MOF	100	83.64	0.179	0.935	6.34	0.997

$$\frac{t}{q_t} = \frac{1}{k_2 q_e^2} + \frac{1}{q_e} t \quad (9)$$

whereas k_1 (min^{-1}) and k_2 (g mol^{-1} min^{-1}) are rate constants corresponding to pseudo-first and pseudo-second orders, respectively, q_e and q_t (mg g^{-1}) represent the quantities of CV dye adsorbed at equilibrium and at time = t, respectively. The models of pseudo-second and pseudo-first orders were obtained by plotting the relation of t/q_t *vs.* t and $\log(q_e - q_t)$ *vs.* t, respectively. From the R^2 values listed in Table 3, we summarized that the uptake process was in great accord with pseudo-second order, which denotes the chemisorption mechanism-controlled rate-determining step (Fig. S6 (ESI)†).

Table 4 shows the thermodynamic characteristics that distinguish the CV adsorption process. As demonstrated by the negative values of ΔG° and ΔH, the adsorption process was endothermic and spontaneous. A positive value of ΔS indicated an improvement in randomness at the solid/solution interface within dye adsorption, which correlates directly to a greater degree of freedom for the adsorbed species.[65] Fig. S7 (ESI)† illustrated the thermodynamic plots of CV dye adsorption onto 25 wt% PWA/Sr-MOF.

3.3.5. Comparison studies of 25 wt% PWA/Sr-MOF with other adsorbents. Table 5 listed different adsorbents for adsorption capacities of CV dye at room temperature compared to 25 wt% PWA/Sr-MOF. From the adsorption results, the modified Sr-MOF adsorbent exhibited a high adsorption capacity between other adsorbents.

Table 4 Thermodynamic parameters form adsorption of CV dye on 25 wt% PWA/Sr-MOF

Temperature (K)	ΔG° (kJ mol^{-1})	ΔS (J mol^{-1} K^{-1})	ΔH (kJ mol^{-1})
298	−167.62		
308	−173.25		
318	−178.8	0.5627	0.0626
328	−184.5		
338	−190.13		

3.4. The catalytic activity of PWA/Sr-MOF

3.4.1. Synthesis of 7-hydroxy-4-methylcoumarin (Pechmann reaction). In a typical reaction, the different molar ratios of resorcinol to ethylacetoacetate (1 : 1, 1 : 1.5, 1 : 2, and 1 : 3) were conducted in presence of 50 mg of the activated catalyst. As illustrated in Fig. 12(a), the yield of formation 7-hydroxy-4-methylcoumarin raised with increasing molar ratio corresponding to ethylacetoacetate then decreased at 1 : 3 molar ratio. The optimum molar ratio was 1 : 2 with a yield of 71.7% using 55 wt% PWA/Sr-MOF. Pure Sr-MOF was slightly active for the synthesis of coumarin, which may be explained by the presence of carboxylic groups in the MOF structure that are characterized by very weak acidity. The varying catalytic activity toward formation coumarin using different five catalysts ascribed to the different PWA content supported on Sr-MOF. Fig. 12(b) shows the generation of the desired product that was enhanced by increasing the PWA content till reached a maximum percentage of 89% using 55 wt% then decreased at higher PWA content. The yield was decreased using higher PWA content (above 55 wt%) because of a decrease in the number of active sites, which is well-matched with the experimental data obtained from the potentiometric titration of the total acidity. Furthermore, the FT-IR spectra of pyridine adsorption confirmed that the B/L ratio reached the maximum in the case of 55 wt% PWA.

Table 5 Comparative maximum adsorption efficiencies of CV dye using different adsorbents (298 K)

Adsorbent	q_m (mg g^{-1})	Ref.
AC-AgNPLs	87.2	66
Chitosan/nanodiopside nanocomposite	104.66	67
Gum arabic-*cl*-poly(acrylamide) nanohydrogel	90.90	68
ZVI-GAM	172.41	69
Chitin nanowhiskers	39.55	70
Zinc oxide nanorods loaded on activated carbon	113.64	71
Surfactant modified magnetic nanoadsorbent	166.66	59
NH_2-MIL-125(Ti) modified SR-MOF	129.87	72
EDTA/corncob	185.19	34
EDTA-GO/corncob	203.90	73
25 wt% PWA-Sr-MOF	230.41	This work

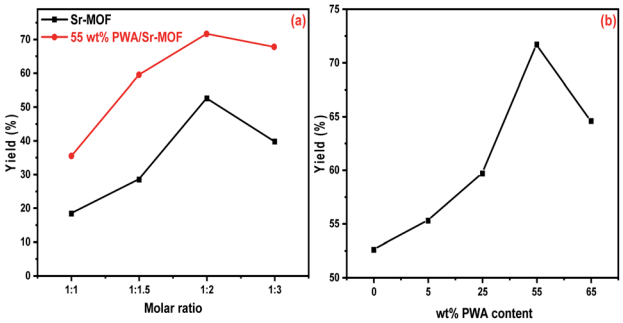

Fig. 12 (a) Effect of resorcinol: ethylacetoacetate molar ratio, [conditions: rpm = 500, dose = 50 mg, time = 120 min and T = 373 K] and (b) effect of PWA content supported on Sr-MOF, [conditions: 1 : 2 resorcinol to ethylacetoacetate molar ratio, rpm = 500, dose = 50 mg, time = 120 min and T = 373 K].

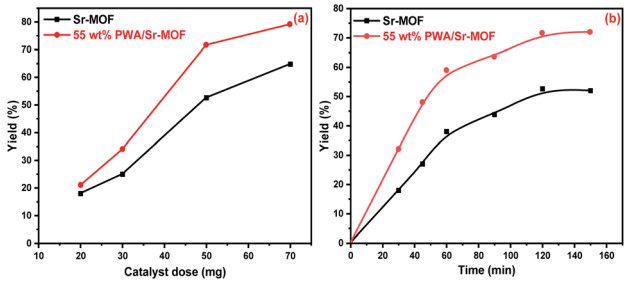

Fig. 13 (a) Effect of catalyst dose, [conditions: 1 : 2 resorcinol to ethylacetoacetate molar ratio, rpm = 500, time = 120 min and T = 373 K] and (b) effect of reaction time in the synthesis of 7-hydroxy-4-methylcoumarin, [conditions: 1 : 2 resorcinol to ethylacetoacetate molar ratio, rpm = 500, dose = 50 mg and T = 373 K].

Using 55 w% PWA/Sr-MOF under identical conditions, the catalytic performance was examined by varying the catalyst dosage between 20 to 70 mg. It is plausible to assume that the raising of the catalyst dosage improved catalytic activity owing to interactions between active sites scattered on the catalyst surface and reactant molecules, as well as the availability of more acidic active sites.[74] The yield of coumarin was enhanced by 8% with increasing the dose from 50 to 70 mg, which revealed that 50 mg was an appropriate mass with excellent yield as observed in Fig. 13(a). The effect of reaction time was investigated under reaction conditions of 50 mg catalyst dose of 55 wt% PWA/Sr-MOF and a molar ratio of 1 : 2 at time intervals from 30 to 150 min. The coumarin yield was raised with reaction time till saturation after 120 min as shown in Fig. 13(b). There was no obvious rise in the product's percentage beyond 150 minutes, indicating that the optimal response time was 120 min. The same behavior was observed in the case of catalyst dose and reaction time effects using pure Sr-MOF catalyst.

3.4.2. Synthesis of 14-phenyl-14*H*-dibenzo[*a*,*j*]xanthene. The catalytic performance of a synthesized xanthene was investigated in a solvent-free environment at 373 K. To optimize the synthesis, we have studied the effect of molar ratio between benzaldehyde and β-naphthol (1 : 1, 1 : 1.5, 1 : 2, and 1 : 3) using 50 mg of pure Sr-MOF and 55 wt% PWA-Sr-MOF catalysts. As observed in Fig. 14(a), the most appropriate molar ratio of

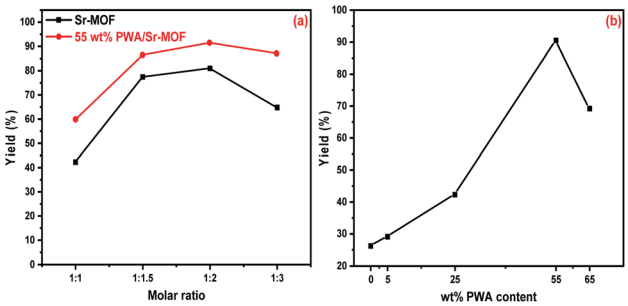

Fig. 14 (a) Effect of benzaldehyde to β-naphthol molar ratio, [conditions: rpm = 500, dose = 50 mg, time = 120 min and T = 373 K] and (b) effect of PWA content supported on Sr-MOF, [conditions: 1 : 2 benzaldehyde to β-naphthol molar ratio, rpm = 500, dose = 50 mg, time = 120 min and T = 373 K].

benzaldehyde to β-naphthol was 1 : 2 with yields of 25.1 and 91.5% for Sr-MOF and 55 wt% PWA-Sr-MOF, respectively.[75] A decrease in catalytic activity was noticed at a molar ratio above 1 : 2, which attributed to the high concentration of β-naphthol frustrated the reaction through blocking the MOF surface active sites. The synthesis of xanthene was highly influenced by the PWA content loaded on Sr-MOF that was improved by increasing the PWA concentration. The yield of the target product increased gradually till reached a maximum of 91.5%

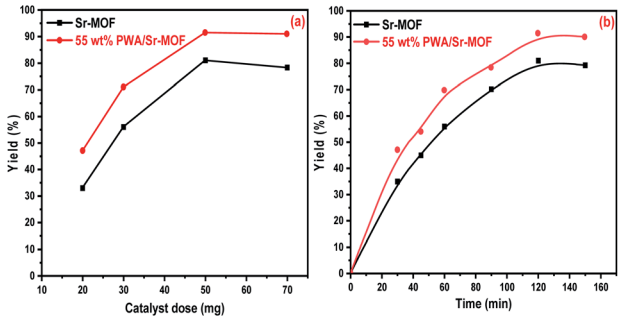

Fig. 15 (a) Effect of catalyst dose, [conditions: 1 : 2 benzaldehyde to β-naphthol molar ratio, rpm = 500, time = 120 min, T = 373 K] and (b) effect of reaction time in the synthesis of xanthene, [conditions: 1 : 2 benzaldehyde to β-naphthol molar ratio, rpm = 500, dose = 50 mg, T = 373 K].

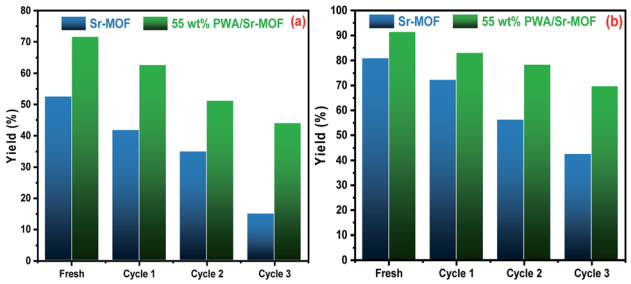

Fig. 16 Catalyst reusability of 55 wt% PWA/Sr-MOF in the synthesis of (a) 7-hydroxy-4-methylcoumarin and (b) 14-phenyl-14*H*-dibenzo[*a*,*j*] xanthene.

for 55 wt% PWA that matched with results from acidity measurements (Fig. 14(b)). The high catalytic activity of catalysts ascribed to the acid sites that densely decorated and expanded on the surface of the frameworks. Additionally, the preparation of xanthene followed Lewis and Brønsted acid sites conventionally.

Various catalyst doses of 20, 30, 50, and 70 mg were examined for the xanthene synthesis under similar circumstances. As illustrated in Fig. 15(a), the yield percentage of xanthene reinforced with high catalyst dose till a maximum value at 50 and 70 mg. As mentioned in coumarin synthesis, the number of acidic active sites distributed in 55 wt% PWA/Sr-MOF increased with high doses of catalyst. At 373 K, the xanthene synthesis was highly influenced by contact reaction time. There was no obvious rise in the product's percentage after 150 minutes, indicating that the optimal response time was 120 minutes (Fig. 15(b)). Using pure Sr-MOF catalyst, the same behaviors were found in terms of catalyst dosage and reaction time effects.

3.4.3. Catalyst reusability. The recyclability of catalyst was studied under optimized reaction conditions using pure Sr-MOF and 55 wt% PWA/Sr-MOF. The catalyst has been removed from the reaction mixture through filteration then washed multiple times with acetone to eliminate any residual product after the reaction completion (120 minutes). Before using the catalyst in the next cycle, it was activated under vacuum at 353 K. The catalytic activity dropped to 44% using 55 wt% PWA/Sr-MOF compared to 15% when it comes to pure Sr-MOF in the case of coumarin synthesis. Furthermore, the catalytic performance on the preparation of xanthene decreased by 21% compared to 38% using 55 wt% PWA/Sr-MOF and Sr-MOF, respectively, after four runs (Fig. 16).

3.4.4. Comparison studies of 55 wt% PWA/Sr-MOF with other catalysts. Tables 6 and 7 compare the catalytic activity of several catalysts on the synthesis of coumarin and xanthene under solvent-free media. In comparison to other produced catalysts, the same 55 wt% PWA/Sr-MOF demonstrated promising catalytic efficiency for both coumarin and xanthene synthesis.

Table 6 Comparison studies of 55 wt% PWA/Sr-MOF with the assistance of other catalysts on Pechmann condensation of resorcinol with ethyl acetoacetate

Entry	Catalyst	Conditions	Time (min)	Yield (%)	Ref.
1	$Zn_{0.925}Ti_{0.075}O$	383 K/solvent-free	180	88.0	33
2	50% PTA/Sn-TiO_2	373 K/solvent-free	120	92.6	76
3	PWA/mont-K10	403 K/solvent-free	480	69.0	77
4	55 wt% PWA/Sr-MOF	373 K/solvent-free	120	71.7	This work

Table 7 Comparison studies of 55 wt% PWA/Sr-MOF with the assistance of other catalysts in the synthesis of 14-aryl-14*H*-dibenzo[*a*,*j*]xanthene

Entry	Catalyst	Conditions	Yield (%)	Time (min)	Ref.
1	$NbCl_5$	Ambient temperature/DCM	95	48(h)	78
2	PVPP-BF_3	373 K/solvent-free	94	90	79
3	ZnO NPs	423 K/ionic liquids	80	60	80
4	$H_5PW_{10}V_2O_{40}$	373 K/solvent free	67	60	81
5	55 wt% PWA/Sr-MOF	373 K/solvent-free	91.5	120	This work

4. Conclusion

In this work, we prepared Sr-MOF based on green aliphatic linkers that were modified by different wt% of PWA. The adsorption efficiency of PWA/Sr-MOF was investigated to remove CV dye from an aqueous medium with a maximum adsorption capacity of 237.0 mg g^{-1}. Different factors have been investigated including solution pH, adsorbent dosage, dye concentration, temperature, and initial dye concentration. Additionally, the catalytic activity of 55 wt% PWA/Sr-MOF was examined for coumarin and xanthene synthesis under solvent-free conditions with yields of 71.7 and 91.5%, respectively. The catalyst showed high catalytic performance after four cycles, which indicates high durability and stability.

Conflicts of interest

There are no conflicts to declare.

References

1 M. Eddaoudi, D. F. Sava, J. F. Eubank, K. Adil and V. Guillerm, Zeolite-like metal–organic frameworks (ZMOFs): design, synthesis, and properties, *Chem. Soc. Rev.*, 2015, **44**, 228–249.

2 J. Lei, R. Qian, P. Ling, L. Cui and H. Ju, Design and sensing applications of metal–organic framework composites, *Trends Anal. Chem.*, 2014, **58**, 71–78.

3 H. W. Langmi, J. Ren, B. North, M. Mathe and D. Bessarabov, Hydrogen Storage in Metal–Organic Frameworks: A Review, *Electrochim. Acta*, 2014, **128**, 368–392.

4 S. S. Han, W.-Q. Deng and W. A. Goddard, Improved designs of metal–organic frameworks for hydrogen storage, *Angew. Chem., Int. Ed.*, 2007, **46**, 6289–6292.

5 C. D. Wu and M. Zhao, Incorporation of Molecular Catalysts in Metal–Organic Frameworks for Highly Efficient Heterogeneous Catalysis, *Adv. Mater.*, 2017, **29**, 1605446.

6 M. S. Adly, S. M. El-Dafrawy, A. A. Ibrahim, S. A. El-Hakam and M. S. El-Shall, Efficient removal of heavy metals from polluted water with high selectivity for Hg(II) and Pb(II) by a 2-imino-4-thiobiuret chemically modified MIL-125 metal–organic framework, *RSC Adv.*, 2021, **11**, 13940–13950.

7 E. López-Maya, C. Montoro, V. Colombo, E. Barea and J. A. R. Navarro, Improved CO_2 Capture from Flue Gas by Basic Sites, Charge Gradients, and Missing Linker Defects on Nickel Face Cubic Centered MOFs, *Adv. Funct. Mater.*, 2014, **24**, 6130–6135.

8 M. A. Lucena, M. F. Oliveira, A. M. Arouca, M. Talhavini, E. A. Ferreira, S. Alves Jr, F. H. Veiga-Souza and I. T. Weber, Application of the Metal–Organic Framework [Eu(BTC)] as a Luminescent Marker for Gunshot Residues: A Synthesis, Characterization, and Toxicity Study, *ACS Appl. Mater. Interfaces*, 2017, **9**, 4684–4691.

9 Y. Pan, Y. Qian, X. Zheng, S.-Q. Chu, Y. Yang, C. Ding, X. Wang, S.-H. Yu and H.-L. Jiang, Precise fabrication of single-atom alloy co-catalyst with optimal charge state for enhanced photocatalysis, *Natl. Sci. Rev.*, 2021, **8**, 1–8.

10 M. F. Sanad, A. R. Puente Santiago, S. A. Tolba, M. A. Ahsan, O. Fernandez-Delgado, M. Shawky Adly, E. M. Hashem, M. Mahrous Abodouh, M. S. El-Shall, S. T. Sreenivasan, N. K. Allam and L. Echegoyen, Co-Cu Bimetallic Metal Organic Framework Catalyst Outperforms the Pt/C Benchmark for Oxygen Reduction, *J. Am. Chem. Soc.*, 2021, **143**, 4064–4073.

11 S. M. F. Vilela, J. A. R. Navarro, P. Barbosa, R. F. Mendes, G. Perez-Sanchez, H. Nowell, D. Ananias, F. Figueiredo, J. R. B. Gomes, J. P. C. Tome and F. A. A. Paz, Multifunctionality in an Ion-Exchanged Porous Metal–Organic Framework, *J. Am. Chem. Soc.*, 2021, **143**, 1365–1376.

12 S. Shalini, V. M. Dhavale, K. M. Eldho, S. Kurungot, T. G. Ajithkumar and R. Vaidhyanathan, 1000-fold enhancement in proton conductivity of a MOF using post-synthetically anchored proton transporters, *Sci. Rep.*, 2016, **6**, 32489.

13 S. N. Zhao, X. Z. Song, M. Zhu, X. Meng, L. L. Wu, S. Y. Song, C. Wang and H. J. Zhang, Assembly of three coordination polymers based on a sulfonic–carboxylic ligand showing high proton conductivity, *Dalton Trans.*, 2015, **44**, 948–954.

14 H. Pham, K. Ramos, A. Sua, J. Acuna, K. Slowinska, T. Nguyen, A. Bui, M. D. R. Weber and F. Tian, Tuning Crystal Structures of Iron-Based Metal–Organic Frameworks for Drug Delivery Applications, *ACS Omega*, 2020, **5**, 3418–3427.

15 X. Li, J. Wu, C. He, Q. Meng and C. Duan, Asymmetric Catalysis within the Chiral Confined Space of Metal–Organic Architectures, *Small*, 2019, **15**, 1804770.

16 P. Garcia-Garcia, M. Muller and A. Corma, MOF catalysis in relation to their homogeneous counterparts and conventional solid catalysts, *Chem. Sci.*, 2014, **5**, 2979–3007.

17 R. Haounati, H. Ouachtak, R. El Haouti, S. Akhouairi, F. Largo, F. Akbal, A. Benlhachemi, A. Jada and A. A. Addi, Elaboration and properties of a new SDS/CTAB@Montmorillonite organoclay composite as a superb adsorbent for the removal of malachite green from aqueous solutions, *Sep. Purif. Technol.*, 2021, **255**, 117335.

18 F. Largo, R. Haounati, S. Akhouairi, H. Ouachtak, R. El Haouti, A. El Guerdaoui, N. Hafid, D. M. F. Santos, F. Akbal, A. Kuleyin, A. Jada and A. A. Addi, Adsorptive removal of both cationic and anionic dyes by using sepiolite clay mineral as adsorbent: experimental and molecular dynamic simulation studies, *J. Mol. Liq.*, 2020, **318**, 114247.

19 K. Gai, A. Avellan, T. P. Hoelen, F. Lopez-Linares, E. S. Hatakeyama and G. V. Lowry, Impact of mercury speciation on its removal from water by activated carbon and organoclay, *Water Res.*, 2019, **157**, 600–609.

20 E. Carvajal-Florez and C.-G. Santiago-Alonso, Technologies applicable to the removal of heavy metals from landfill leachate, *Environ. Sci. Pollut. Res.*, 2019, **26**, 15725–15753.

21 S. Rodriguez-Mozaz, M. J. de Alda and D. Barcelo, Monitoring of estrogens, pesticides and bisphenol A in natural waters and drinking water treatment plants by solid-phase extraction-liquid chromatography-mass spectrometry, *J. Chromatogr. A*, 2004, **1045**, 85–92.

22 A. Lerch, S. Panglisch, P. Buchta, Y. Tomita, H. Yonekawa, K. Hattori and R. Gimbel, Direct river water treatment using coagulation/ceramic membrane microfiltration, *Desalination*, 2005, **179**, 41–50.

23 M. S. Adly, S. M. El-Dafrawy and S. A. El-Hakam, Application of nanostructured graphene oxide/titanium dioxide composites for photocatalytic degradation of rhodamine B and acid green 25 dyes, *J. Mater. Res. Technol.*, 2019, **8**, 5610–5622.

24 B. P. Chaplin, Critical review of electrochemical advanced oxidation processes for water treatment applications, *Environ. Sci.: Processes Impacts*, 2014, **16**, 1182–1203.

25 W. S. Abo El-Yazeed, S. A. El-Hakam, A. A. Salah and A. A. Ibrahim, Fabrication and characterization of reduced graphene-$BiVO_4$ nanocomposites for enhancing visible light photocatalytic and antibacterial activity, *J. Photochem. Photobiol., A*, 2021, **417**, 113362.

26 H. Ouachtak, R. El Haouti, A. El Guerdaoui, R. Haounati, E. Amaterz, A. A. Addi, F. Akbal and M. L. Taha, Experimental and molecular dynamics simulation study on the adsorption of rhodamine B dye on magnetic montmorillonite composite γ-Fe_2O_3@Mt, *J. Mol. Liq.*, 2020, **309**, 113142.

27 R. Haounati, A. El Guerdaoui, H. Ouachtak, R. El Haouti, A. Bouddouch, N. Hafid, B. Bakiz, D. M. F. Santos, M. Labd Taha, A. Jada and A. Ait Addi, Design of direct Z-scheme superb magnetic nanocomposite photocatalyst Fe_3O_4/Ag_3PO_4@Sep for hazardous dye degradation, *Sep. Purif. Technol.*, 2021, **277**, 119399.

28 F. Alakhras, E. Alhajri, R. Haounati, H. Ouachtak, A. A. Addi and T. A. Saleh, A comparative study of photocatalytic degradation of rhodamine B using natural-based zeolite composites, *Surf. Interfaces*, 2020, **20**, 100611.

29 J. Yang, B. Hou, J. Wang, B. Tian, J. Bi, N. Wang, X. Li and X. Huang, Nanomaterials for the Removal of Heavy Metals from Wastewater, *Nanomaterials*, 2019, **9**, 424.

30 M. R. Kulkarni, T. Revanth, A. Acharya and P. Bhat, Removal of crystal violet dye from aqueous solution using water hyacinth: equilibrium, kinetics and thermodynamics study, *Resour.-Effic. Technol.*, 2017, **3**, 71–77.

31 S. R. Patil, S. S. Sutar and J. P. Jadhav, Sorption of crystal violet from aqueous solution using live roots of eichhornia crassipes: kinetic, isotherm, phyto and cyto-genotoxicity studies, *Environ. Technol. Innovation*, 2020, **18**, 100648.

32 S. Bouasla, J. Amaro-Gahete, D. Esquivel, M. I. Lopez, C. Jimenez-Sanchidrian, M. Teguiche and F. J. Romero-Salguero, Coumarin Derivatives Solvent-Free Synthesis under Microwave Irradiation over Heterogeneous Solid Catalysts, *Molecules*, 2017, **22**, 2072.

33 N. H. Jadhav, S. S. Sakate, N. K. Rasal, D. R. Shinde and R. A. Pawar, Heterogeneously Catalyzed Pechmann Condensation Employing the Tailored $Zn_{0.925}Ti_{0.075}O$ NPs: Synthesis of Coumarin, *ACS Omega*, 2019, **4**, 8522–8527.

34 A. A. Napoleon and F.-R. Nawaz Khan, Potential anti-tubercular and *in vitro* anti-inflammatory agents: 9-substituted 1,8-dioxo-octahydroxanthenes through cascade/domino reaction by citric fruit juices, *Med. Chem. Res.*, 2014, **23**, 4749–4760.

35 M. Bitaraf, A. Amoozadeh and S. Otokes, Nano-WO_3-Supported Sulfonic Acid: A Versatile Catalyst for the One-Pot Synthesis of 14-Aryl-14*H*-dibenzo[*a*,*j*]xanthene Derivatives Under Solvent-Free Conditions, *Proc. Natl. Acad. Sci., India, Sect. A*, 2019, **89**, 437–443.

36 Y. Cao, C. Yao, B. Qin and H. Zhang, Solvent-free synthesis of 14-aryl-14*H*-dibenzo[*a*,*j*]xanthenes catalyzed by recyclable and reusable iron(III) triflate, *Res. Chem. Intermed.*, 2013, **39**, 3055–3062.

37 I. Yoon, J. Z. Li and Y. K. Shim, Advance in photosensitizers and light delivery for photodynamic therapy, *Clin. Endosc.*, 2013, **46**, 7–23.

38 A. B. Ormond and H. S. Freeman, Dye Sensitizers for Photodynamic Therapy, *Materials*, 2013, **6**, 817–840.

39 V. S. R. Ganga, M. K. Choudhary, R. Tak, P. Kumari, S. H. R. Abdi, R. I. Kureshy and N.-u. H. Khan, Epoxides as a new feedstock for the synthesis of xanthene derivatives by using highly efficient, reusable tungstated zirconia heterogeneous catalyst, *Catal. Commun.*, 2017, **94**, 5–8.

40 W. S. Abo El-Yazeed, Y. G. Abou El-Reash, L. A. Elatwy and A. I. Ahmed, Facile fabrication of bimetallic Fe–Mg MOF for the synthesis of xanthenes and removal of heavy metal ions, *RSC Adv.*, 2020, **10**, 9693–9703.

41 S. M. El-Dafrawy, R. S. Salama, S. A. El-Hakam and S. E. Samra, Bimetal-organic frameworks (Cu_x-Cr_{100-x}-MOF) as a stable and efficient catalyst for synthesis of 3,4-dihydropyrimidin-2-one and 14-phenyl-14*H*-dibenzo[*a*,*j*] xanthene, *J. Mater. Res. Technol.*, 2020, **9**, 1998–2008.

42 T. Preočanin, A. Selmani, P. Lindqvist-Reis, F. Heberling, N. Kallay and J. Lützenkirchen, Surface charge at Teflon/aqueous solution of potassium chloride interfaces, *Colloids Surf., A*, 2012, **412**, 120–128.

43 S. Pornsatitworakul, B. Boekfa, T. Maihom, P. Treesukol, S. Namuangruk, S. Jarussophon, N. Jarussophon and J. Limtrakul, The coumarin synthesis: a combined experimental and theoretical study, *Monatsh. Chem.*, 2017, **148**, 1245–1250.

44 Y. Du, P. Yang, S. Zhou, J. Li, X. Du and J. Lei, Direct synthesis of ordered meso/macrostructured phosphotungstic acid/SiO_2 by EISA method and its catalytic performance of fuel oil, *Mater. Res. Bull.*, 2018, **97**, 42–48.

45 K. Wu, C. Du, F. Ma, Y. Shen and J. Zhou, Optimization of metal–organic (citric acid) frameworks for controlled release of nutrients, *RSC Adv.*, 2019, **9**, 32270–32277.

46 A. E. R. S. Khder, H. M. A. Hassan and M. S. El-Shall, Acid catalyzed organic transformations by heteropoly tungstophosphoric acid supported on MCM-41, *Appl. Catal., A*, 2012, **411–412**, 77–86.

47 X. Yang, L. Qiao and W. Dai, One-pot synthesis of a hierarchical microporous-mesoporous phosphotungstic acid-HKUST-1 catalyst and its application in the selective oxidation of cyclopentene to glutaraldehyde, *Chin. J. Catal.*, 2015, **36**, 1875–1885.

48 D. J. Martin, K. Qiu, S. A. Shevlin, A. D. Handoko, X. Chen, Z. Guo and J. Tang, Highly efficient photocatalytic H_2 evolution from water using visible light and structure-controlled graphitic carbon nitride, *Angew. Chem., Int. Ed.*, 2014, **53**, 9240–9245.

49 D. Jiang, Y. Chen, N. Li, W. Li, Z. Wang, J. Zhu, H. Zhang, B. Liu and S. Xu, Synthesis of Luminescent Graphene Quantum Dots with High Quantum Yield and Their Toxicity Study, *PLoS One*, 2015, **10**, 1–15.

50 Y. Wang, S. Zuo, J. Yang and S. H. Yoon, Evolution of Phosphorus-Containing Groups on Activated Carbons during Heat Treatment, *Langmuir*, 2017, **33**, 3112–3122.

51 A. Márquez-Herrera, V. M. Ovando-Medina, B. E. Castillo-Reyes, M. Zapata-Torres, M. Meléndez-Lira and J. González-Castañeda, Facile Synthesis of $SrCO_3$-$Sr(OH)_2$/PPy Nanocomposite with Enhanced Photocatalytic Activity under Visible Light, *Materials*, 2016, **9**, 30.

52 L. J. Wang, H. Deng, H. Furukawa, F. Gándara, K. E. Cordova, D. Peri and O. M. Yaghi, Synthesis and Characterization of Metal–Organic Framework-74 Containing 2, 4, 6, 8, and 10 Different Metals, *Inorg. Chem.*, 2014, **53**, 5881–5883.

53 S. A. El-Hakam, A. A. Ibrahim, L. A. Elatwy, W. S. A. El-Yazeed, R. S. Salama, Y. G. A. El-Reash and A. I. Ahmed, Greener route for the removal of toxic heavy metals and synthesis of 14-aryl-14*H* dibenzo[*a*,*j*]xanthene using a novel and efficient Ag–Mg bimetallic MOF as a recyclable heterogeneous nanocatalyst, *J. Taiwan Inst. Chem. Eng.*, 2021, **122**, 176–189.

54 C. Freitas, N. S. Barrow and V. Zholobenko, Accessibility and Location of Acid Sites in Zeolites as Probed by Fourier Transform Infrared Spectroscopy and Magic Angle Spinning Nuclear Magnetic Resonance, *Johnson Matthey Technol. Rev.*, 2018, **62**, 279–290.

55 I. Khalil, H. Jabraoui, G. Maurin, S. Lebègue, M. Badawi, K. Thomas and F. Maugé, Selective Capture of Phenol from Biofuel Using Protonated Faujasite Zeolites with Different Si/Al Ratios, *J. Phys. Chem. C*, 2018, **122**, 26419–26429.

56 A. A. Ibrahim, R. S. Salama, S. A. El-Hakam, A. S. Khder and A. I. Ahmed, Synthesis of sulfated zirconium supported MCM-41 composite with high-rate adsorption of methylene blue and excellent heterogeneous catalyst, *Colloids Surf., A*, 2021, **616**, 126361.

57 L. M. Cotoruelo, M. D. Marqués, F. J. Díaz, J. Rodríguez-Mirasol, J. J. Rodríguez and T. Cordero, Lignin-based activated carbons as adsorbents for crystal violet removal from aqueous solutions, *Environ. Prog. Sustainable Energy*, 2012, **31**, 386–396.

58 L. d. S. Silva, J. d. O. Carvalho, R. D. d. S. Bezerra, M. S. d. Silva, F. J. L. Ferreira, J. A. Osajima and E. C. d. S. Filho, Potential of Cellulose Functionalized with Carboxylic Acid as Biosorbent for the Removal of Cationic Dyes in Aqueous Solution, *Molecules*, 2018, **23**, 743.

59 C. Muthukumaran, V. M. Sivakumar and M. Thirumarimurugan, Adsorption isotherms and kinetic studies of crystal violet dye removal from aqueous solution using surfactant modified magnetic nanoadsorbent, *J. Taiwan Inst. Chem. Eng.*, 2016, **63**, 354–362.

60 Q. Meng, X. Xin, L. Zhang, F. Dai, R. Wang and D. Sun, A multifunctional Eu MOF as a fluorescent pH sensor and exhibiting highly solvent-dependent adsorption and degradation of rhodamine B, *J. Mater. Chem. A*, 2015, **3**, 24016–24021.

61 P. S. Ghosal and A. K. Gupta, Determination of thermodynamic parameters from Langmuir isotherm constant-revisited, *J. Mol. Liq.*, 2017, **225**, 137–146.

62 S. E. Subramani and N. Thinakaran, Isotherm, kinetic and thermodynamic studies on the adsorption behaviour of textile dyes onto chitosan, *Process Saf. Environ. Prot.*, 2017, **106**, 1–10.

63 J.-P. Simonin, On the comparison of pseudo-first order and pseudo-second order rate laws in the modeling of adsorption kinetics, *Chem. Eng. Sci.*, 2016, **300**, 254–263.

64 H. Ouachtak, A. El Guerdaoui, R. Haounati, S. Akhouairi, R. El Haouti, N. Hafid, A. Ait Addi, B. Šljukić, D. M. F. Santos and M. L. Taha, Highly efficient and fast batch adsorption of orange G dye from polluted water using superb organo-montmorillonite: experimental study and molecular dynamics investigation, *J. Mol. Liq.*, 2021, **335**, 116560.

65 P. Joshi and S. Manocha, Kinetic and thermodynamic studies of the adsorption of copper ions on hydroxyapatite nanoparticles, *Mater. Today*, 2017, **4**, 10455–10459.

66 A. H. AbdEl-Salam, H. A. Ewais and A. S. Basaleh, Silver nanoparticles immobilised on the activated carbon as efficient adsorbent for removal of crystal violet dye from aqueous solutions. A kinetic study, *J. Mol. Liq.*, 2017, **248**, 833–841.

67 S. G. Nasab, A. Semnani, A. Teimouri, M. J. Yazd, T. M. Isfahani and S. Habibollahi, Decolorization of crystal violet from aqueous solutions by a novel adsorbent chitosan/nanodiopside using response surface methodology and artificial neural network-genetic algorithm, *Int. J. Biol. Macromol.*, 2019, **124**, 429–443.

68 G. Sharma, A. Kumar, M. Naushad, A. García-Peñas, A. a. H. Al-Muhtaseb, A. A. Ghfar, V. Sharma, T. Ahamad and F. J. Stadler, Fabrication and characterization of Gum arabic-*cl*-poly(acrylamide) nanohydrogel for effective adsorption of crystal violet dye, *Carbohydr. Polym.*, 2018, **202**, 444–453.

69 J. Liu, Y. Wang, Y. Fang, T. Mwamulima, S. Song and C. Peng, Removal of crystal violet and methylene blue from aqueous solutions using the fly ash-based adsorbent material-supported zero-valent iron, *J. Mol. Liq.*, 2018, **250**, 468–476.

70 S. Gopi, A. Pius and S. Thomas, Enhanced adsorption of crystal violet by synthesized and characterized chitin nano whiskers from shrimp shell, *J. Water Process. Eng.*, 2016, **14**, 1–8.

71 E. A. Dil, M. Ghaedi, A. Ghaedi, A. Asfaram, M. Jamshidi and M. K. Purkait, Application of artificial neural network and response surface methodology for the removal of crystal violet by zinc oxide nanorods loaded on activate carbon: kinetics and equilibrium study, *J. Taiwan. Inst. Chem. Eng.*, 2016, **59**, 210–220.

72 G. Wen and Z. Guo, Facile modification of NH_2-MIL-125(Ti) to enhance water stability for efficient adsorptive removal of crystal violet from aqueous solution, *Colloids Surf., A*, 2018, **541**, 58–67.

73 H. Wang, X. Lai, W. Zhao, Y. Chen, X. Yang, X. Meng and Y. Li, Efficient removal of crystal violet dye using EDTA/graphene oxide functionalized corncob: a novel low cost adsorbent, *RSC Adv.*, 2019, **9**, 21996–22003.

74 H. Naeimi and Z. S. Nazifi, Sulfonated diatomite as heterogeneous acidic nanoporous catalyst for synthesis of 14-aryl-14*H*-dibenzo[*a*,*j*]xanthenes under green conditions, *Appl. Catal., A*, 2014, **477**, 132–140.

75 W. S. Abo El-Yazeed, M. Eladl, A. I. Ahmed and A. A. Ibrahim, Sulfamic: acid incorporated tin oxide: acidity and activity relationship, *J. Alloys Compd.*, 2021, **858**, 158192.

76 S. M. Hassan, A. I. Ahmed and M. A. Mannaa, Surface acidity, catalytic and photocatalytic activities of new type $H_3PW_{12}O_{40}$/Sn-TiO_2 nanoparticles, *Colloids Surf., A*, 2019, **577**, 147–157.

77 B. Vijayakumar and G. Ranga Rao, PWA/montmorillonite K10 catalyst for synthesis of coumarins under solvent-free conditions, *J. Porous Mater.*, 2011, **19**, 233–242.

78 A. Andrade Bartolomeu, M. Menezes and L. Silva Filho, Efficient one-pot synthesis of 14-aryl-14*H*-dibenzo[*a*,*j*]xanthene derivatives promoted by niobium pentachloride, *Chem. Pap.*, 2014, **68**, 1593–1600.

79 M. Mokhtary and S. Refahati, Polyvinylpolypyrrolidone-supported boron trifluoride (PVPP-BF_3): mild and efficient catalyst for the synthesis of 14-aryl-14*H*-dibenzo[*a*,*j*]xanthenes and bis(naphthalen-2-yl-sulfane) derivatives, *Dyes Pigm.*, 2013, **99**, 378–381.

80 G. B. Dharma Rao, M. P. Kaushik and A. K. Halve, An efficient synthesis of naphtha[1,2-*e*]oxazinone and 14-substituted-14*H*-dibenzo[*a*,*j*]xanthene derivatives promoted by zinc oxide nanoparticle under thermal and solvent-free conditions, *Tetrahedron Lett.*, 2012, **53**, 2741–2744.

81 R. Tayebee and S. Tizabi, Highly Efficient and Environmentally Friendly Preparation of 14-Aryl-14*H* dibenzo[*a*,*j*]xanthenes Catalyzed by Tungsto-divanado-phosphoric Acid, *Chin. J. Catal.*, 2012, **33**, 962–969.